Monthly Notices of the ROYAL ASTRONOMICAL SOCIETY

MNRAS **443,** 58–66 (2014) doi:10.1093/mnras/stu1135

Periodic radio variabilities of the blazar 1156+295: harmonic oscillations

Jun-Yi Wang,[1,2] Tao An,[3,4]★ Willem A. Baan[3] and Xiang-Long Lu[2]

[1]*School of Mathematics and Computing Science, Xiangtan University, Hunan 411105, China*
[2]*Key Laboratory of Cognitive Radio & Information Processing, Guilin University of Electronic Technology, Guilin 541004, China*
[3]*Shanghai Astronomical Observatory, Chinese Academy of Sciences, 200030 Shanghai, China*
[4]*Key Laboratory of Radio Astronomy, Chinese Academy of Sciences, 210008 Nanjing, China*

Accepted 2014 June 5. Received 2014 May 30; in original form 2014 January 21

ABSTRACT

(Quasi)-periodic oscillations of the radio luminosity of a typical blazar 1156+295 were analysed to investigate the dynamic processes associated with the central engine of the active galactic nucleus. Three numerical techniques, the Lomb–Scargle periodogram, the Weighted Wavelet *Z*-transform and the improved Phase Dispersion Minimization, were used to search for candidate periodicities in the radio light curves of 1156+295 at 14.5, 8.0 and 4.8 GHz. The results of these methods are consistent with the detection of four periodic components with characteristic periods of ∼1.7 (P_4), ∼2.4 (P_3), ∼3.4 (P_2) and ∼7.5 yr (P_1), which suggest a harmonic relationship in frequency of 4: 3: 2: 1 with f_1 as the fundamental frequency. Except for the fact that P_1 persistently shows in the whole time span, the three others appear intermittent and are only prominent during certain time ranges. The second harmonic mode (P_2) is most powerful at all three observing frequency bands. The multiplicity and harmonic relation of the periodicities in 1156+295 reconfirms that global p-mode oscillations of the accretion disc are coupled to the jet. The oscillation of the disc is likely driven by Kelvin–Helmholtz instabilities in the inner edge of the accretion disc.

Key words: methods: statistical – galaxies: active – quasars: individual: 1156+295.

1 INTRODUCTION

Active galactic nuclei (AGN) are powered by the accretion process of the supermassive black holes (SMBH) located in the heart of the galaxies. The production and release of the energy from the AGN remains still an open question although the discovery of AGN traces back 50 years. A major difficulty in understanding black hole (BH) accretion is that the central engine of the AGN cannot be spatially resolved by any existing astronomical facilities. Even very long baseline interferometry (VLBI), which provides the highest resolution imaging technique in observational astronomy, does not provide sufficient resolution to map the power source of the AGN. This puzzle may be solved by using non-imaging techniques such as time series analysis that is used widely in studies of variable astronomical objects. The variability carries plenty of information about the structure and energy changes occurring at the centre of the sources.

Blazars, as a subgroup of AGN, are prominent for their rapid and significant variability at all wavelengths, which makes them excellent targets for investigating AGN physics. The time-scales of the flux density variation of blazars range from years to hours. Some blazars show evidence of quasi-periodic oscillations of the total flux density on time-scales of a few years (e.g. Sillanpaa et al. 1988; Lehto & Valtonen 1996; Sillanpaa al. 1996). The periodic variability is thought to be closely related to the dynamic precesses in the BH accretion disc system. Possible driving mechanisms include jet precession in a binary SMBH system (e.g. Villata et al. 1998), orbital motion of hotspots around the SMBH (Broderick & Loeb 2006), or global oscillations of the accretion disc (e.g. Rubio-Herrera & Lee 2005a,b). Since the flux density variation of blazars is rather easily observed with single telescope monitoring, many blazar monitoring programs have been made at radio, optical and X-ray wavelengths. Radio emission of blazars is generally thought to arise from relativistic jets that are beamed towards the observer. The variability time-scales, the spectral index changes, the polarization angle changes, the multiband variability correlations, and the time delays derived from the variability studies of blazars provide ample information to locate the emitting region and to identify the nature of the luminous nuclear emission.

The blazar 1156+295 (4C+29.45 at $z = 0.729$) shows significant variability throughout the electromagnetic spectrum from radio to gamma-rays (Hong et al. 2004, and references therein). Owing to its notable variability, 1156+295 is an excellent template for investigating the variability of nuclear emissions. Blazar 1156+295 is among the sample monitored bi-weekly since 1980 by the 26-m radio telescope of the University of Michigan Radio Astronomy Observatory (UMRAO) at 4.8, 8.0 and 14.5 GHz (Aller et al. 1985).

★ E-mail: antao@shao.ac.cn

The UMRAO light curves show many drastic events during the past three decades with durations of several months (Kovalev et al. 2002; Hong et al. 2004). After 1995, this source entered an extraordinarily active phase with five major flares between 1995 and 2010, each separated roughly by 3.4 yr and showing a double-peak pattern with a separation of ∼1 yr, of which the reliability and physical nature remains unclear (Hong et al. 2004). Compared with the variability at centimetre wavelengths, the flux density at millimetre wavelengths show much stronger variations (Bower et al. 1997; Wehrle et al. 1998). The kpc- and pc-scale morphological properties of the radio emission of 1156+295 have been analysed in the framework of a helical jet model using high-resolution multi-epoch and multifrequency VLBI, VLBI Space Observatory Program (VSOP), Multi-Element Radio-Linked Interferometer Network and Very Large Array observations made over a period of 50 months (Hong et al. 2004). Strong radio flares are possibly correlated with the ejection of new jet components (Bower et al. 1997; Piner & Kingham 1997; Zhao et al. 2011).

Intense radio flux density monitoring of 1156+295 shows variability on time-scales of hours, known as intraday variability (IDV), with a largest amplitude variation of 40 per cent (Lovell et al. 2003; Savolainen & Kovalev 2008; Kuchibhotla 2010). The IDV characteristics in 1156+295 were also detected at optical bands (Wills et al. 1983, 1992). The IDV in 1156+295 at centimetre wavelengths is thought to result from interstellar scintillation by a nearby, highly turbulent scattering screen (Savolainen & Kovalev 2008). In addition, Tornikoski et al. (1994) found a correlation of the variabilities in the optical and radio bands when comparing the light curves obtained with the 76-cm optical reflector at the Rosemary Hill Observatory (USA) with the radio light curves from the Metsähovi Radio Research Station (Finland) (at 22 and 37 GHz) and the Swedish-ESO Submillimetre Telescope (Chile) (at 90 GHz). Gamma-ray variability of an order of magnitude has been detected using the Energetic Gamma Ray Experiment Telescope (EGRET) onboard the Compton Gamma Ray Observatory (Hartman et al. 1999), which has been confirmed recently by the *Fermi* gamma-ray telescope (Abdo et al. 2009).

The periodic variability behaviour of 1156+295 has been investigated by Hovatta et al. (2007) using the Lomb–Scargle (LS) periodogram method on data obtained from the Metsähovi Radio Observatory at 22 and 37 GHz. They identified a significant periodic signal on a time-scale of 3.29 yr, and a similar time-scale of 3.49 yr was derived from the Discrete Correlation Function method. They presented further evidence of three other periodic components with one longer and two shorter time-scales in the LS periodogram, although Hovatta et al. (2007) did not comment on these weaker periodicities. Hovatta, Lehto & Tornikoski (2008) also re-analysed the same radio light curves of 1156+295 with the windowed Fourier transform technique, and they detected two periodic components on time-scales of 3.4 and 1.7 yr, respectively. These two periodic signals are only prominent in the second half of the time series, i.e. from 1995 to 2005.

In this paper, we will re-investigate the variability of 1156+295 in order to identify periodicities in the radio light curves and to establish a harmonic relation between these periodicities. The presence of harmonics in 1156+295 would reinforce that harmonic periodicities are a common characteristic of blazar variability. The harmonic variability reveals the dynamics of the nuclear system and signifies the connection between driving oscillations in the accretion disc and variability of the blazar jet. This renewed study is different and more complete than previous research (e.g. Hovatta et al. 2007, 2008) because current radio data have a longer time coverage, more

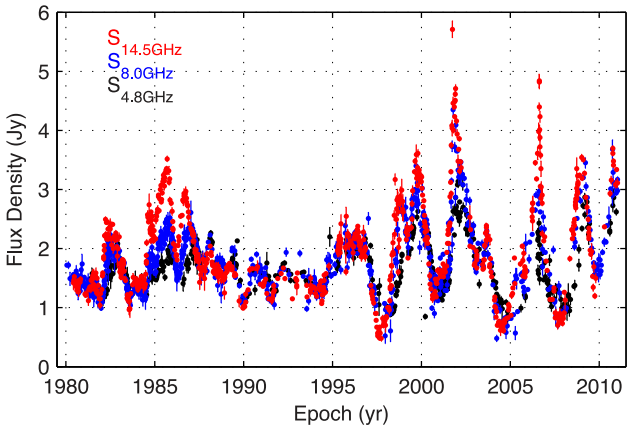

Figure 1. Light curves of 1156+295 at 14.5 GHz (red), 8.0 GHz (blue) and 4.8 GHz (black).

Table 1. Observing logs of the UMRAO data.

Freq. (GHz)	Start date	End date	Duration (yr)	Number
4.8	1981 May 16	2010 Dec. 17	29.59	482
8.0	1977 May 25	2011 Jan. 10	33.63	900
14.5	1980 June 05	2011 Jan. 06	30.59	786

data points, and a better regularity of the time sampling. Three numerical methods have been employed to identify periodicities in the radio light curves of 1156+295: the LS periodogram method, the Weighted Wavelet *Z*-transform (WWZ) method, and the Phase Dispersion Minimization (PDM) method.

The structure of the paper is as follows: Section 2 describes the observational data used for the periodicity analysis; Section 3 introduces the basic principle and the algorithms of the LS, PDM and WWZ methods, and presents the periodicity analysis results; and Section 4 presents the discussion and Section 5 summarizes the conclusions.

2 OBSERVATIONAL DATA

This paper focuses on an investigation of the periodicities of blazar 1156+295 in the radio bands. The total flux density monitoring data were obtained from the UMRAO at 4.8, 8.0, 14.5 GHz. Fig. 1 displays the light curves with fairly uniform sampling and without large gaps. Table 1 presents the observational logs covering a total time span of about 30 years. The average sampling interval is about two weeks for 14.5- and 8.0-GHz data, and 26 d for 4.8-GHz data. Noting that the previous research reported a most significant period of 3.4 yr (Hovatta et al. 2008), the bi-weekly time sampling is good enough for finding year-time-scale periodicities. And the light curves have sufficiently long time coverage to search for any periodic signals on time-scales of a few years with several complete cycles.

3 PERIODICITY SEARCHES

Three methods have been used to search for periodicities in the radio light curves of 1156+295. (1) The LS periodogram method (Lomb 1976; Scargle 1982) is a modified periodogram technique with improved performance of analysing unevenly spaced time series. It is a frequency-domain method based on the *discrete Fourier transform* (DFT). (2) The WWZ method (Daubechies 1990; Kaiser & Hudgins

1995; Foster 1996) is a periodicity analysis technique in both the time and frequency domains. Compared to the conventional wavelet transform (WT), the WWZ is more efficient to handle irregularly sampled variability data by introducing the weighted projection of the light curves on trial functions. (3) The PDM method (Stellingwerf 1978; Schwarzenberg-Czerny 1997; Stellingwerf 2011) is a time-domain analysis method, belonging to the class of data folding techniques. Different from the first two methods, PDM is a non-parametric method that does not require a priori models or trial functions. Each method has its own advantages and the independent use of different methods is important for verifying the reliability of the detected periodicities.

3.1 Lomb–Scargle periodogram

In Fourier theory, a time series of magnitude or luminosity can be represented by power as a function of frequency. A least-squares fitting to the light curves with a linear combination of sine and cosine functions with varying frequencies indicates the frequency at which the power becomes strongest. Previous research have proved that, if the time series data are equally spaced in time, the standard DFT technique is an excellent tool for periodicity searching. However, the astronomical time series are often unevenly sampled due to various reasons, e.g., finite telescope time availability, bad weather conditions, intermittent flares, and obscuration by the Sun.

When a Fourier transform is applied to irregularly sampled data, the irregularity of the time interval gives rise to a more complex spectrum than the one derived from regularly sampled data. For instance, uneven time sampling may induce spurious and lead to a shift of the peak relative to the genuine frequency/period (Scargle 1982). Moreover, each true peak in the spectrum produces a number of aliases of various amplitudes distributed throughout the spectrum. The confusion arising from the aliases of the major peak makes the identification of secondary periodic signals rather difficult.

A modified periodogram (LS periodogram) was proposed to eliminate the aliasing problem caused by unevenly sampled data (e.g. Lomb 1976; Scargle 1982). The LS periodogram extracts the mean value of the signal and employs a phase shift of the basis functions. The resulting normalized periodogram does not require interpolating of missing data, avoiding the spurious artificial peaks. The calculation of the transform coefficients is insensitive to time shifts. The normalized power in the periodogram $P(\omega)$ at a characteristic frequency ω (and period $T = 2\pi/\omega$) is defined as the inverse of the variance of the fit to the data as a function of the trial frequency. The most probable period corresponds to the one with the maximum power $P(\omega)$. Further details of the LS methodology may be found in An et al. (2013), which presents an analysis of the periodicities in the blazar NRAO 530.

The periodograms for the time series of 1156+295 as presented in Fig. 2 show a good agreement with each other. The strongest peak corresponding to a characteristic frequency of $\sim$0.30 yr^{-1}, or a period P_2 of $\sim$3.3 yr (the candidate periodicities are labelled in ascending frequency sequence). The peaks at frequencies $\sim$0.13 yr^{-1} (period $P_1 = 7.5$ yr) and $\sim$0.42 yr^{-1} (period $P_3 = 2.4$ yr) have almost equivalent powers, but they have not been reported in previous research. The distribution of the light curve data is rather uniform and the light curves have no large gaps and the lower amplitude peaks of P_1 and P_3 are not symmetric with respect to P_2. Therefore, P_1 and P_3 should not be simply aliases of the primary peak P_2. Their appearance in all three light curves reinforces the detection of two new candidate periodicities.

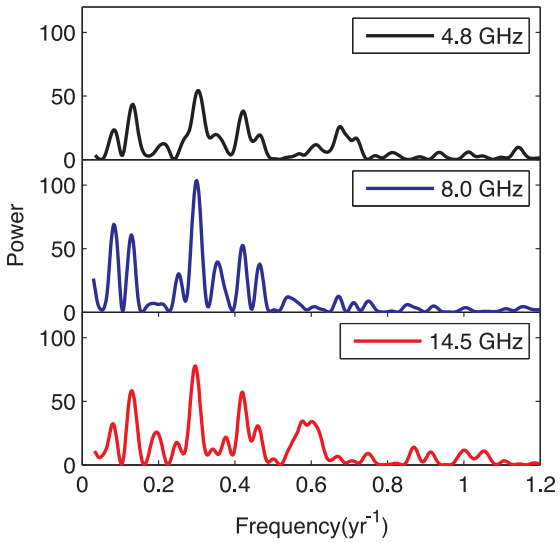

Figure 2. LS periodograms of 1156+295. The peaks of the power spectrum density correspond to the characteristic frequencies.

Table 2. Periods derived from the LS periodogram.

Freq (GHz)	Label	Period (yr)	Frequency (yr^{-1})	Power
4.8	(P_0)	11.72	0.085	23.2826
	P_1	7.49	0.134	43.4973
	P_2	3.28	0.305	54.1381
	P_3	2.37	0.422	38.2512
	P_4	1.48	0.676	25.9943
8.0	(P_0)	12.06	0.083	69.1207
	P_1	7.78	0.129	60.7675
	P_2	3.33	0.300	103.4976
	P_3	2.38	0.420	52.6179
14.5	(P_0)	12.29	0.081	32.3708
	P_1	7.69	0.130	58.4873
	P_2	3.37	0.297	77.8832
	P_3	2.38	0.420	57.3506
	P_4	1.73	0.578	34.5381

Note. The periodic component in the bracket means this feature is probably an artefact due to red noise (see discussion in Section 4).

At the low-frequency end, there is a peak corresponding to a frequency of 0.083 yr^{-1} (period of about 12.0 yr). This component is only strong in the 8.0-GHz periodogram. At 14.5 GHz, there is a hint of a broad frequency component at 0.603 yr^{-1} (period $P_4 = 1.67$ yr), which is not evident at 4.8 and 8.0 GHz. Except for these five candidate periodicities, the remaining peaks seem to be contaminated by the side lobes of the prominent P_2 and P_3 components. Table 2 lists the candidate periods in the LS periodogram.

In above LS periodogram, the measurement uncertainties were not taken into account. Measurement errors are usually included in the variance calculations in the form of weighting. A generalized Lomb–Scargle (GLS) periodogram which takes the error as weighting was also employed to search for periodicities. The results are compared in Fig. 3. The obvious changes are: (1) in the GLS plot, P_3 (2.4 yr, $f = 0.42$ yr^{-1}) is only evident in 4.8 GHz, but not obvious in 8.0 and 14.5 GHz; (2) in the GLS plot, P_2 (3.3 yr, $f = 0.3$ yr^{-1}) at 4.8 GHz shows a broad peak. Except those, there are no

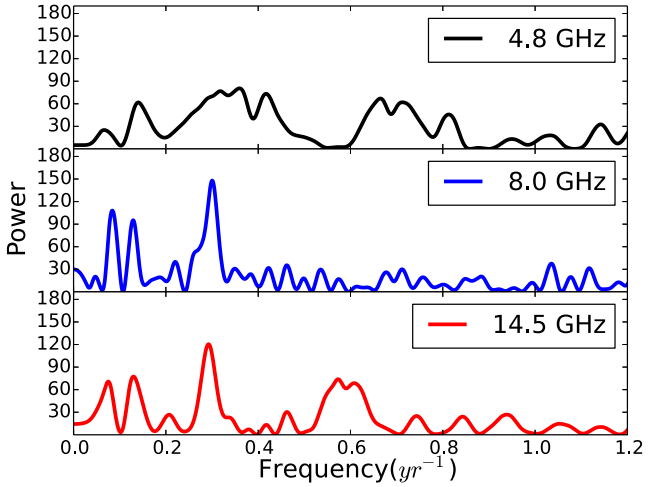

Figure 3. GLS periodograms of 1156+295.

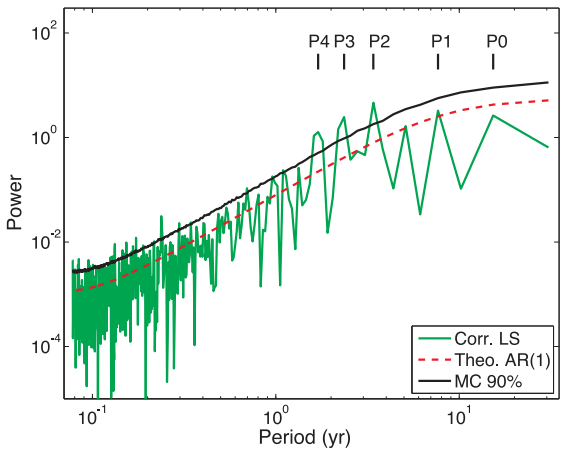

Figure 4. Comparison between the LS periodogram and red noise spectrum. The (red) dashed line represents the theoretical red noise spectrum, while the (green) solid line represents the LS periodogram. The solid (black) line represents 90 per cent Monte Carlo confidence level.

substantial differences in other frequency components. The unremarkable changes are not surprising because the weighting slightly changes the light curves. Compared to no weighting or uniform weighting used in the canonical LS, the GLS used $W = 1/\sigma^2$ for the data points. The 4.8-GHz light curves have relatively larger fractional error, hence the spectrum (Fig. 3) becomes more noisy. Some intermittent or short-lived frequency components such as P_3 are easily washed out in the global fit to the whole time series. Considering the general consistency between the results with and without weighting, we would keep the LS periodogram in following statistical significance analysis.

Astronomical periodicities are often contaminated by random noise, so it is important to discriminate genuine periodic components (caused by ordered physical processes) from non-periodic ones (caused by stochastic processes). White noise results from measurement errors and is commonly seen in natural processes. White noise unlikely leads to large peaks in the periodograms because its power is equally distributed in frequency space. Therefore, a component with a significant peak can be unambiguously attributed to a true periodicity. However, the AGN light curve is time related and differs from random noise, because adjacent data points in the time sequence have an internal relation with each other. Such time-correlated physical processes can give rise to frequency-dependent variability with a power spectrum that has a strong correlation between the power and frequency.

On the other hand, AGN light curves commonly exhibit a frequency-dependent red noise component with a power spectrum $P \propto f^{-\alpha}$ with index $\alpha = 1$–2. When the time span of the light curve is only a few times that of the period to be searched, the red noise in the data may generate large stochastic peaks in the low frequency (or long-period) domain. Red noise easily results from stochastic processes in a jet plasma or an accretion flow.

A comparison between the observed LS periodogram and a simulated red noise spectrum has been presented in Fig. 4. The diagram contains the theoretical red noise spectrum generated by a first-order autoregressive process AR(1), the LS periodogram, and the 90 per cent confidence level obtained from 1000 Monte Carlo test runs. More details of the modelling and the procedure of red noise spectrum may be found in the discussion of variability of NRAO 530 (An et al. 2013). Five peaks corresponding to the periodicities detected in Section 3 are labelled. Three peaks (P_2, P_3, P_4) are above the 90 per cent MC confidence level. A pure red noise model cannot explain these periodicities and these three are unlikely to be generated by stochastic process. On the other hand, P_0 lies below the theoretical AR(1) spectrum and is most likely caused by red noise.

3.2 Weighted wavelet *Z*-transform

In the LS periodogram method discussed above, a time series is fitted with a combination of sine and cosine functions. By definition, these trigonometric functions have infinite dimensions which give unavoidable problems for global fitting of time series with finite length. If the data are also sparsely distributed, the discontinuity at the gaps may induce spurious spikes in the power spectrum.

A further shortcoming of the Fourier transform methodology is that it loses the localized properties of the periodicities, since the least-squares fit is made for the whole time series. This problem becomes more evident when the possible periods and their amplitudes vary with time. A Fourier transform of a blazar light curve containing intermittent periodic components may thus smear those short-duration components over the whole time span.

This WT methodology can identify the localized properties in both time and frequency domains by evaluating a time series within an appropriate time window and then searching for frequency components within each window separately. Because the window width in the WT is scalable, it becomes more flexible and efficient than a *windowed Fourier transform*. By choosing windows of different sizes, the WT produces multiple resolutions in both time and frequency; large windows may be used to identify global properties, while small windows identify the detailed characters of transient or short-duration components. More importantly, the WT methodology can analyse time series that contain non-stationary power at multiple different frequencies (Daubechies 1990).

The procedure of the periodicity analysis by using the WT is (1) choose a mother wavelet and set a series of *scale frequencies* ω (test frequencies) and *positions* τ (time shifts) to analyse; (2) for a certain *scale frequency*, convolve the wavelet function with the data at every *position* τ (time shift) along the time series and obtain a series of power spectra for that *scale* frequency; (3) repeat step (2) for each *scale frequency* ω and obtain wavelet spectra for each *scale* ω and *position* τ. The most frequently used wavelet function is the Morlet wavelet (Grossmann & Morlet 1984).

The WT can represent the time series by using a model function $y(t)$ consisting of a series of trial functions $\varphi(t)$: $y(t) = \sum_a y_a \varphi_a(t)$ ($a = 1, 2$,É), where y_a is the coefficient for each trial function. Three trial functions are used all the time: $\varphi_1(t) = \mathbf{1}(t)$, $\varphi_2(t) = \cos(\omega(t-\tau))$, $\varphi_3(t) = \sin(\omega(t-\tau))$, where the constant function has been introduced to reduce the artificial peaks in wavelet spectrum resulting from an unevenly sampled time series (Foster 1996).

The incorporation of a weighted projection of the time series data on to the three trial functions with statistical weights $w_a = e^{-c\omega^2(t-\tau)^2}$ ($a = 1, 2, 3$) enhances the ability to detect periodicities and provides a statistical description of the detected periodic signals. The addition of *Z*-statistics serves to correct for a bias towards lower frequencies resulting from sampling a wider window and more data points at lower frequencies (Foster 1996). A more extensive description of this *WWZ* methodology has been presented in An et al. (2013).

The WWZ period search of 1156+295 was limited to the frequency range of 0.033–100 yr^{-1}. The minimal frequency corresponds to a longest time-scale of about 30 yr, which corresponds to a single cycle during the whole observing span. The maximal frequency corresponds to a shortest time-scale of 4 d that equals one sixth of the bin size. A frequency step of 0.000 001 yr^{-1} is adopted, resulting in 65 536 test frequencies. A decay constant $c = 0.0075$ is used to define the width of the wavelet window. Too high a value of c gives a rapid decay of the WWZ power and results in a failure to identify periodicities with small amplitude oscillations.

The three WWZ power spectra as a function of time and frequency are shown in Fig. 5 exhibit similar appearance. The x-axis represents the characteristic periods, and the y-axis the observing time. Periodic behaviour is evident as a pattern spanning a certain time range at a given frequency. A persistent periodicity P_1 (∼7.7 yr) is distinctly detected in all three plots. A semipersistent periodicity P_0 (∼13.0 yr) is found to be weaker than P_1 at 14.5 and 4.8 GHz, but stronger than P_1 at 8.0 GHz. This result is consistent with the LS periodogram. The centre lines of the P_0 and P_1 contours show some variation with time, which could be an artefact caused by mode interactions between P_0 and P_1.

In addition to the persistent periodicities, some prominent periodic components appear during shorter time intervals, where they dominate the total spectrum power. For example, the periods P_2 and P_3 are blended during the period 1978–1987, they are weak during 1988–1992, and after 1992 they become the first and second brightest components. The peak of P_2 (∼3.3 yr) happens around 1997 at 14.5 and 8 GHz, and around 2000 at 4.8 GHz. The time span of 1992–2011 covers 6 complete cycles of P_2. The character of period P_2 is consistent with the previous WT analysis of an independent data set at 22 GHz (Hovatta et al. 2008). P_3 (∼2.2 yr) is the secondary strongest component in the current 14.5-GHz WWZ spectrum after 2005. Besides period P_3 there is also a weak component identified as P_4 (1.6 yr) in the 14.5 GHz spectrum. At two lower observing bands 4.8 and 8.0 GHz, the P_3 and P_4 are not significant because of opacity effects that smear out short-lived high-frequency oscillations. The 4.8-GHz spectrum shows a hint of P_4 around 2003, but is invisible in the 8.0 GHz spectrum. The LS periodogram (Fig. 2) only marginally identifies the P_4 component in the 14.5 GHz spectrum. In summary, five candidate periodicities are detected in the WWZ power spectra; their period and duration are listed in Table 3.

Fig. 6 shows the statistical significance of the detected periodicities based on Monte Carlo simulations. A total 5000 simulated time series of red noise type were generated, having the same sampling number, overall time scan, sampling intervals. We run WWZ for each time series using the same setup for the observed light curve. At the position corresponding to the peak of P_1 shown in Fig. 5, we recorded the power in each WWZ spectrum of simulated light curve. Then the resulting 5000 power values were put together and shown in a histogram plot in Fig. 6. The percentage number in each panel shows the ratio of the accumulated occurrence number of powers exceeding the observed value to the total test number 5000. That

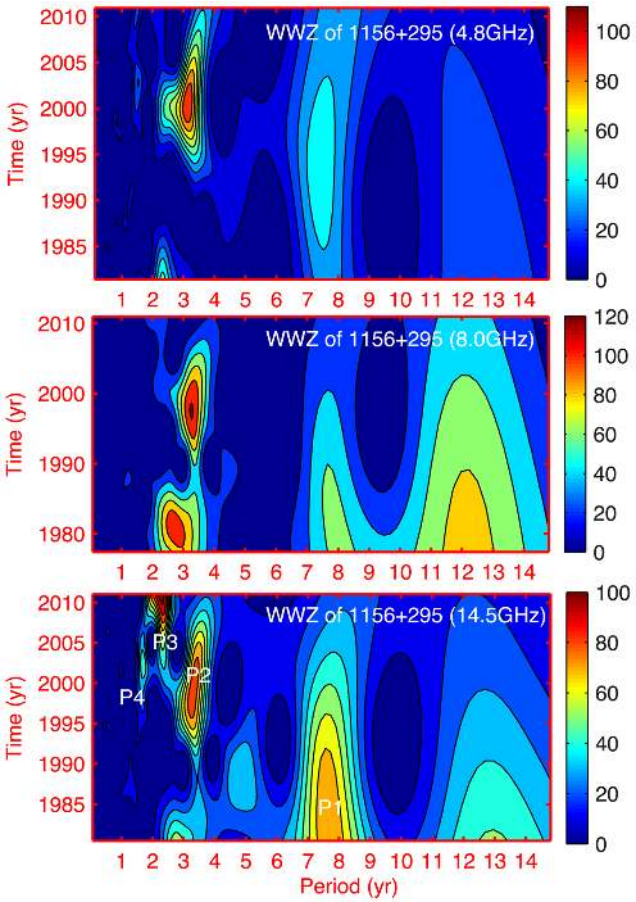

Figure 5. WWZ power spectra. From top to bottom, 4.8, 8.0 and 14.5 GHz. The colour scale represents the WWZ power of a certain period at a given time.

Table 3. Periodicity derived from the WWZ.

ν (GHz)	Name	Period (yr)	Begin time t_b	End time t_e	Number of cycles
4.8	(P_0)	12.4	1981.37	2010.96	3
	P_1	7.4	1981.37	2010.96	4
	P_2	3.1	1991.11	2010.96	7
	P_4	1.6	1996.03	2011.03	8
8.0	(P_0)	12.2	1977.39	2011.03	2
	P_1	8.0	1977.39	2011.03	4
	P_2	3.3	1990.07	2010.96	7
	P_3	2.2	1977.39	2011.03	4
14.5	(P_0)	12.5	1980.42	2011.02	2
	P_1	7.7	1980.42	2011.02	4
	P_2	3.3	1980.42	2011.02	8
	P_3	2.2	2002.14	2011.02	4
	P_4	1.6	1992.35	2011.03	12

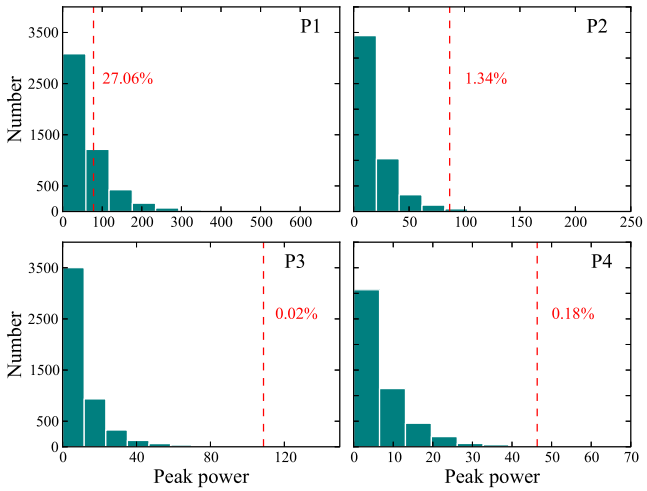

Figure 6. Statistical significance of WWZ-detected periods. The simulations were made by using the 14.5 GHz data. The *x*-axis represents the peak power of simulated periodograms at the periodicity. The vertical dashed line indicates the peak power detected in the WWZ power spectrum for each periodic component. The *y*-axis gives the occurrence number. The percentage number gives the probability that the periodicity could be generated by random noise.

corresponds to a probability that the observed periodicity is a fake detection that may result from random red noise in the light curve. P_2, P_3 and P_4 have a high statistical confidence; it is consistent with that they are the strongest components in the WWZ spectrum. The lowest frequency component P_1 with 27.06 per cent is more affected by the red noise that becomes stronger at low frequency domain.

3.3 Phase dispersion minimization of 1156+295

The PDM methodology is essentially a data folding technique. It first folds the data according to a trial period, then examines the variance within the phase bin (Stellingwerf 1978; Schwarzenberg-Czerny 1997) for that trial period. The trial period giving the minimal variance is identified as a candidate. The PDM method is a non-parametric method that does not necessarily assume a (fixed) trigonometric (trial) function for the trial period and determines periodic components from data sets with erratic time intervals, poor time coverage, non-sinusoid shapes, and even with large noise components.

Assuming that there are N data points $\{(x_i, t_i)|i = 1, \ldots N\}$, the variance σ^2 can be calculated as

$$\sigma^2 = \frac{\sum (x_i - \bar{x})^2}{N - 1}, \tag{1}$$

where $\bar{x} = \sum x_i / N$ is the mean of the observed data. The principle of the PDM is to compare the data with the mean light curve and minimize the variance of the data. Let Π be the trial period, then the phase vector ϕ of each data point is given by

$$\phi_i = t_i / \Pi - [t_i / \Pi], \phi_i \in [0, 1]. \tag{2}$$

The data are grouped into M samples in such a way: in each sample j, the data points have similar phase. Note that the phase space (0,1) is divided into fixed bins, but the choice of the samples is more flexible. A data point can be placed into many samples. The sample variance s_j^2 ($j = 1, \ldots, M$) has the same form as equation (3) and gives a measure of the scatter of the data points around

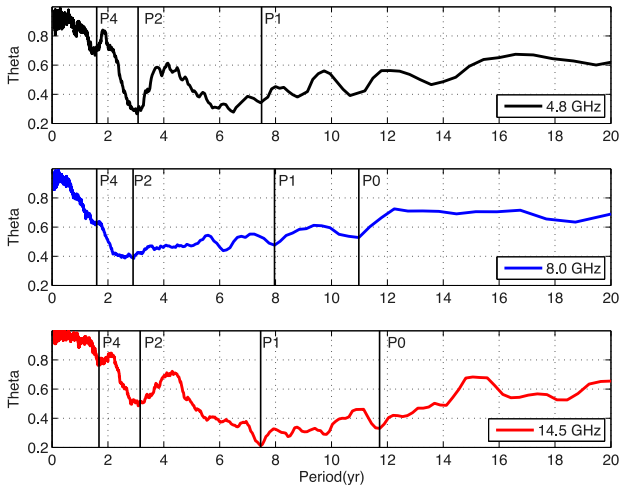

Figure 7. Θ–period diagrams for PDM method: 4.8 GHz (top), 8.0 GHz (middle) and 14.5 GHz (bottom).

the mean light curve in each sample. The overall variance for all samples is expressed as (Stellingwerf 1978)

$$s^2 = \frac{\sum (n_j - 1) s_j^2}{\sum n_j - M}, \tag{3}$$

where n_j is the number of data points in the jth phase bin.

A statistical variable Θ is used to evaluate the reliability of the trial period (Stellingwerf 1978):

$$\Theta = s^2 / \sigma^2, \Theta \in [0, 1]. \tag{4}$$

The PDM searches for a series of test periods. If the trial period Π is not a true period, then $s^2 \approx \sigma^2$ and $\Theta \approx 1$. On the other hand, if Π is a true period, then Θ will reach a local minimum compared with neighbouring test periods, and in the ideal case Θ becomes zero for a genuine period. Mathematically, PDM is a least-square fit of the data to a model curve (i.e. the mean light curve), which is similar to the Fourier transform, except that the PDM model curve can have any form and it is not necessarily sinusoidal. The Θ statistics is expressed as (Schwarzenberg-Czerny 1997):

$$P\left(\Theta \frac{d_0}{d_2} u\right) = I\left(\frac{d_2}{2}, \frac{d_1}{2}; u\right), \tag{5}$$

where $0 < u < 1$, $d_0 = n - 1$, $d_1 = r - 1$, $d_2 = n - r$ give the corresponding numbers of the degrees of freedom, n is the number of observed data values and r is the number of subsets.

Period searching with the PDM algorithm has been carried out in two steps: (1) divide the data into a number of coarse segmentations. The PDM performs a broad search for periodicities after the data gaps were removed and generates a group of candidate periodicities. (2) Re-compute the segmented data using the a 'fine step' PDM to search for periodicities near the candidates derived from the first step. This second 'fine scan' step produces more accurate frequency components. The two-step procedure produces more accurate frequency components and results in a higher computing speed than blind searches with uniform period step (Lu et al. 2012).

The total time interval of the time series of 1156+295 is about 30 yr and in order to find year-time-scale periodicities, trial frequencies were set in the range from 0.05 to 1 (yr^{-1}) (corresponding to trial period range of 1–20 years). The Θ–period relations at three observing frequencies with the PDM technique are shown in Fig. 7, where each local minimum of Θ corresponds to a possible

Table 4. Periodicity analysis results from PDM.

ν (GHz)	Name	Freq. (yr^{-1})	Period (yr)	Θ_{min}	Significance Monte Carlo
4.8	P_1	0.1333	7.5	0.338	99.56 per cent
	P_2	0.3226	3.1	0.325	99.68 per cent
	P_4	0.6250	1.6	0.722	98.50 per cent
8.0	(P_0)	0.0917	10.9	0.521	98.70 per cent
	P_1	0.1282	7.8	0.474	99.65 per cent
	P_2	0.3448	2.9	0.389	99.72 per cent
	P_4	0.6667	1.5	0.617	98.80 per cent
14.5	(P_0)	0.0862	11.6	0.333	99.62 per cent
	P_1	0.1333	7.5	0.215	99.65 per cent
	P_2	0.3226	3.1	0.486	99.41 per cent
	P_4	0.6250	1.6	0.755	98.50 per cent

periodicity. At 14.5 GHz, the primary minimum of Θ corresponds to a period of $\sim$7.5 yr (P_1), which has also been detected in the LS and WWZ power spectra. However, the period P_1 is not very prominent in the 4.8- and 8-GHz Θ–period diagrams. Period P_0, which has been seen in the LS and WWZ spectra, is also detected by the PDM, but at lower periods of 11.6 yr (14.5 GHz), 10.9 yr (8.0 GHz). At 4.8 GHz, the identification of P_0 is not easy because there are three local minima at 8.8 yr, 10.7 yr and 13.6 yr with equivalent Θ values. The most significant component at 4.8 and 8.0 GHz is period P_2 of 3.1 yr, which is also evident at 14.5 GHz. P_4 shows as a local minimum around period of 1.6 yr. On the other hand, periodicity P_3, which is detected from both LS and WWZ methods, does not appear in the PDM diagrams. In addition, there is a trough around $P \sim 6.1$ yr at 4.8 and 8.0 GHz. This suspicious component was not detected by the LS and WWZ methods, and it is also not clear in the 14.5-GHz PDM diagram.

In order to evaluate the statistical significance of these candidate periods, Monte Carlo tests have been run. The significance of each periodicity is expressed as a percentage in the last column in Table 4. Both P_1 and P_2 have $\sim 3\sigma$ significance.

4 DISCUSSION

4.1 Harmonic periodic oscillations

Periodic oscillations have been detected in the blazar 1156+295 from the radio light curves with time-scales of 1.7 and 3.4 yr (Hovatta et al. 2007, 2008). The main purpose of this paper is to verify these periodicities using a different data base and to search for new periods. Three numerical methods, working differently and independently, provide a consistent conclusion that there exist multiple periodicities (Section 3). Besides the two earlier known periodicities of 3.4 and 1.7 yr, two additional periods of 2.3 and 7.7 yr have been identified. Although there are some reports of multiple variability periods in blazars, the sample size is still quite small (Kelly et al. 2003; Hovatta et al. 2008). Multiple periods provide a better understanding of the variability phenomena.

The detected periods in 1156+295 show an interesting harmonic relation (Table 5). The frequency ratio of P_2 (3.4 yr), P_3 (2.4 yr) and P_4 (1.7 yr) is almost exactly 2: 3: 4. That suggests a fundamental frequency of 0.147 yr^{-1}, corresponding to a period of 6.8 yr. In the LS and WWZ spectra, the putative 6.8 yr component is not seen, but a 7.5-yr feature (P_1) is quite obvious. The shift towards lower frequency (or higher period) of P_1 is likely attributed to the influence by the neighbour component P_0 which is generated by red noise. In the following, it will be assumed that P_1 represents the fundamental oscillation period of 6.8 yr, albeit with a slight deviation from the anticipated.

Multiple harmonic oscillations were also observed in other blazars, such as 3C 279 (Liu, Zhao & Wu 2006), 1510−089 (Xie et al. 2008) and NRAO 530 (An et al. 2013). They have a common feature that the lowest order harmonics is often persistent but not prominent, while the second- or third-order harmonics are enhanced during the active periods of radio outbursts. The stability and persistence of this fundamental mode reflects the fact that it is tightly related to the underlying jet flow.

4.2 Physical driving mechanism

Detection of quasi-periodic oscillations in blazar light curves is of great importance to the study of the AGN dynamics. Periodic radio variability from relativistic jet in blazars could be related to the ordered changes of the properties; for example, the propagation of a shock along a helical trajectory may result in periodic change of the Doppler boosting factor (Rieger 2004). The 1156+295 jet does show such a helically twist morphology on parsec scales (Hong et al. 2004; Zhao et al. 2011).

A helical jet scenario may reveal details about (1) the jet precession driven by SMBH binaries or warped accretion discs, or (2) the Kelvin–Helmholtz (K-H) instability originated in the accretion disc and propagating into the jet flow. Although the variability time-scales is comparable with the precessing period of the jets which are of the order of years (Kudryavtseva et al. 2011; Caproni, Abraham & Montiero 2013; Beaklini & Abraham 2014), jet precession cannot satisfactorily explain the multiple periods derived from the present observations. Moreover, K-H instabilities in the boundary

Table 5. Periodicities detected with the LS, WWZ and PDM techniques.

Method	Frequency (GHz)	Detected period (yr)	Detected frequency (yr^{-1})	Frequency[a] ratio
LS	4.8	1.5, 2.4, 3.3, 7.5, (11.7)	0.6763, 0.4220, 0.3052, 0.1334, (0.0853)	4.6: 2.9: 2.1: 0.9 (:0.6)
	8.0	. . . , 2.4, 3.3, 7.8, (12.1)	. . . . . , 0.4221, 0.3006, 0.1285, (0.0829)	. . . 2.9: 2.0: 0.9: (:0.6)
	14.5	1.7, 2.4, 3.4, 7.5, (12.3)	0.6029, 0.4198, 0.2969, 0.1334, (0.0814)	4.1: 2.9: 2.0: 0.9 (:0.6)
WWZ	4.8	1.6,. . . , 3.1, 7.4, (12.4)	0.6250,. . . . . , 0.3226, 0.1351, (0.0806)	4.3:. . . 2.2: 0.9 (:0.5)
	8.0	. . . , 2.2, 3.3, 8.0, (12.2)	. . . . . , 0.4545, 0.3030, 0.1250, (0.0819)	. . . 3.1: 2.1: 0.9 (:0.6)
	14.5	1.6, 2.2, 3.3, 7.7, (12.5)	0.6250, 0.4545, 0.3030, 0.1299, (0.0800)	4.3: 3.1: 2.1: 0.9 (:0.5)
PDM	4.8	1.6,. . . , 3.1, 7.5,. . .	0.6250,. . . . . , 0.3226, 0.1333,. . .	4.3:. . . 2.2: 0.9
	8.0	1.5,. . . , 2.9, 7.8, (10.9)	0.6667,. . . . . , 0.3448, 0.1282, (0.0917)	4.5:. . . 2.3: 0.9 (:0.6)
	14.5	1.6,. . . , 3.1, 7.5, (11.6)	0.6250,. . . . . , 0.3226, 0.1333, (0.0862)	4.3:. . . 2.2: 0.9 (:0.6)

[a]The frequency ratio is calculated with the fundamental frequency of 0.1447 yr^{-1}.

of the jet flow or possibly kink instabilities may periodically change the beaming of the radiation pattern of the jet but will not produce multiple periods either.

Alternatively, variations in the accretion processes and the dynamics of the disc may produce the quasi-periodic variations, assuming that these variations propagate into the properties of the jet and the observed brightness of the radio source. King et al. (2013) have suggested that the Lense–Thirring precession mechanism of a geometrically thick accretion torus, invoked to explain quasi-periodic oscillations (QPOs) in microquasars, may also be at work in the blazar J1359+401, which has a much longer QPO period. Magnetically choking of the accretion flow in general relativistic 3D magnetohydro-dynamic simulations are found to produce quasi-period variations of the energy outflow efficiency of the relativistic jets (Tchekhovskoy, Narayan & McKinney 2011). The dominant mode of these fluctuations has a period of the order of one day for a massive BH (King et al. 2013). In addition, accretion flow instabilities in the radiation-pressure-dominated inner regions of the disc may create high surface density (slowly accreting) and low surface density rings in the disc (Lightman & Eardley 1974). The estimated time-scales for this process are much too long for all observed QPO sources (Meier 20012; King et al. 2013). Alternatively, such density rings may be formed on a thermal time-scale in the inner disc giving a QPO time-scale of ≈0.2 yr, which would be adequate for the long-period QPOs of sources like J1359+4011 (King et al. 2013). All these processes are accommodated by the complexity of the accretion discs for massive BH systems and may indeed facilitate variations of accretion flow and the energy flux of the jet with comparable periods. However, they would have difficulty to explain harmonics of the year-scale oscillations as observed in 1156+295 and NRAO 530.

On the other hand, global p-mode oscillations in a thick disc may produce the observed period characteristic of 1156+295. While both thin and thick accretion discs can oscillate quasi-periodically, only the oscillation of a thick disc can be global and trigger long-term quasi-periodic accretion with harmonic frequencies (e.g. Rezzolla et al. 2003; Zanotti, Rezzolla & Font 2003). Coupling between the quasi-periodic variation of the accretion flow and the plasma injection at the launching of the jet will result in variations of the energy flux of the radio jet (Falcke & Biermann 1995; Marscher et al. 2002). The observed oscillation frequency constrains the outer radius of the thick disc for a known BH mass (Liu et al. 2006). For 1156+295 the mass of the SMBH has been estimated at $4.3 \times 10^8\,M_\odot$ (Pian, Falomo & Treves 2005), which places a lower limit of the outer radius to be $1000 \times r_G = 1.27 \times 10^{17}$ cm, where r_G is the Schwarzschild radius. The quasi-periodic variation of the plasma injection will be superposed on the more steady (large-scale) injections resulting from major accretion events associated producing the large radio outbursts of 1156+295.

However, there is no clear evidence yet about the exact trigger for the oscillations in the accretion process. The excitation of global p-mode oscillation may result from global perturbation or from a local and periodic agent. One simplified possibility is that the K-H instabilities in the inner disc trigger the disc oscillation and these periodic oscillations propagate from the inner to the outer part of the disc.

5 CONCLUSION

Three methods have been used to analyse the characteristic periodicity embedded in the radio light curves of the blazar 1156+295: the LS, WWZ, and PDM methods. The major results can be summarized as follows.

(1) All together five periodicities are detected. A significance analysis made with Monte Carlo tests identifies four as true periods, and the remaining long-period one is probably an artefact resulting from red noise.

(2) The main results obtained from the three methods show excellent consistency, proving the validity of these numerical techniques in the AGN variability study. Compared with LS and PDM, the WWZ displays more details of the variability, showing the persistence and intermittence of the periods and their time evolution. In particular, the localization advantage of the wavelet method allows us to verify short-lived periodic components, which are often smeared in a global fit of the whole time series.

(3) The oscillation frequencies of the periodicities display a harmonic relation, 1:2:3:4, with a fundamental frequency of $\sim 0.147\ \mathrm{yr}^{-1}$ (or a period of ∼6.8 yr). P_1 corresponds to the fundamental frequency although it is a bit larger than the expected value, due to the contamination from the neighbour red noise artefact. P_2, P_3 and P_4 represent the 2nd, 3rd and 4th harmonics, respectively. Continuation of the flux density monitoring using large sensitive telescope such as the newly built Shanghai Tian Ma (65-m) telescope would check if there exist even higher mode harmonics.

(4) Blazar 1156+295 is one of the few quasars showing persistent periodic variability. The multiplicity and harmonic relation of the long-term periodicities in 1156+295 re-confirm the similar findings in three other blazars 3C 279 (Liu et al. 2006), 1510−089 (Xie et al. 2008) and NRAO 530 (An et al. 2013) and suggests that these harmonic relations are characteristic for all blazars. The existence of these harmonic relations indicate that the radio variability result from the dynamics of the accretion disc, such that p-mode oscillations of the accretion disc (e.g. Liu et al. 2006) propagate into the blazar jet and cause the variability. The investigation of a larger sample of blazars in order to establish their harmonic periodicity behaviours in a statistical manner would further improve the understanding of the disc–jet coupling in AGN.

ACKNOWLEDGEMENTS

This work was supported by the China Ministry of Science and Technology (grant no. 2013CB837900), the Strategic Priority Research Programme on Space Science of the Chinese Academy of Sciences (XDA04060700), the National Science Foundation of China (11261140641, U61261017, U1331205), the Chinese Academy of Sciences (KJZD-EW-T01). WAB has been supported as a Visiting Professor of the Chinese Academy of Sciences. The University of Michigan Radio Astronomy Observatory is supported by funds from the NSF, NASA, and the University of Michigan.

REFERENCES

Abdo A. A. et al., 2009, ApJS, 183, 46
Aller H. D., Aller M. F., Latimer G. E., Hodge P. E., 1985, ApJS, 59, 513
An T., Baan W. A., Wang J.-Y., Wang Y., Hong X.-Y., 2013, MNRAS, 434, 3487
Beaklini P. P. B., Abraham Z., 2014, MNRAS, 437, 489
Bower G. C., Backer D. C., Wright M., Forster J. R., Aller H. D., Aller M. F., 1997, ApJ, 484, 118
Broderick A. E., Loeb A., 2006, MNRAS, 367, 905
Caproni A., Abraham Z., Montiero H., 2013, MNRAS, 428, 280
Daubechies I., 1990, IEEE Trans. Inf. Theory, 36, 961
Falcke H., Biermann P. L., 1995, A&A, 293, 665

Foster G., 1996, AJ, 112, 1709
Grossmann A., Morlet J., 1984, SJAM J. Math. Anal., 15, 723
Hartman R. C. et al., 1999, ApJS, 123, 79
Hong X. Y., Sun C. H., Zhao J. -H., Jiang D. R., Shen Z. -Q., An T., Wang W. H., Yang J., 2004, A&A, 417, 887
Hovatta T., Tornikoski M., Lainela M., Lehto H. J., Valtaoja E., Torniainen I., Aller M. F., Aller H. D., 2007, A&A, 469, 899
Hovatta T., Lehto H. J., Tornikoski M., 2008, A&A, 488, 897
Kaiser G., Hudgins L. H., 1995, Phys. Today, 48, 57
Kelly B. C., Hughes P. A., Aller H. D., Aller M. F., 2003, ApJ, 591, 695
King O. G. et al., 2013, MNRAS, 436, L114
Kovalev Y. Y., Kovalev Y. A., Nizhelsky N. A., Bogdantsov A. B., 2002, PASA, 19, 83
Kuchibhotla H. S., 2010, PhD thesis, Purdue University
Kudryavtseva N. A. et al., 2011, A&A, 526, 51
Lehto H. J., Valtonen M. J., 1996, ApJ, 460, 207
Lightman A. P., Eardley D. M., 1974, ApJ, 187, L1
Liu F. K., Zhao G., Wu X. B., 2006, ApJ, 650, 749
Lomb N. R., 1976, Astrophys. Space Sci., 39, 447
Lovell J. E. J., Jauncey D. L., Bignall H. E., Kedziora-Chudczer L., Macquart J.-P., Rickett B. J., Tzioumis A. K., 2003, ApJ, 126, 1699
Lu J.-C., Wang J.-Y., An T., Lin J.-M., Qiu H.-B., 2012, Res. Astron. Astrophys., 12, 643
Marscher A., Jorstad S. G., Gomez J. L., Aller M. F., Tersranta H., Lister M. L., Stirling A. M., 2002, Nature, 417, 625
Meier D. L., 2012, Black Hole Astrophysics: The Engine Paradigm. Springer-Verlag, Berlin
Pian E., Falomo R., Treves A., 2005, MNRAS, 361, 919
Piner B. G., Kingham K. A., 1997, ApJ, 485, L61
Rezzolla L., Yoshida S., Maccarone T. J., Zanotti O., 2003, MNRAS, 344, L37
Rieger F. M., 2004, ApJ, 615, L5
Rubio-Herrera E., Lee W. H., 2005a, MNRAS, 357, L31
Rubio-Herrera E., Lee W. H., 2005b, MNRAS, 362, 789
Savolainen T., Kovalev Y. Y., 2008, A&A, 489, L33
Scargle J. D., 1982, ApJ, 263, 835
Schwarzenberg-Czerny A., 1997, ApJ, 489, 941
Sillanpaa A., Haarala S., Valtonen M. J., Sundelius B., Byrd G. G., 1988, ApJ, 325, 628
Sillanpaa A. et al., 1996, A&A, 315, L13
Stellingwerf R. F., 1978, AJ, 224, 953
Stellingwerf R. F., 2011, Solar Stellar Astrophys., 5, 47
Tchekhovskoy A., Naryan R., McKinney J. C., 2011, MNRAS, 418, L79
Tornikoski M., Valtaoja E., Terasranta H., Smith A. G., Nair A. D., Clements S. D., Leacock R. J., 1994, A&A, 289, 673
Villata M., Raiteri C. M., Sillanpaa A., Takalo L. O., 1998, MNRAS, 293, L13
Wehrle A. E. et al., 1998, ApJ, 497, 178
Wills B. J. et al., 1983, ApJ, 274, 62
Wills B. J., Wills D., Breger M., Antonucci R. R. J., Barvainis R., 1992, ApJ, 398, 454
Xie G. Z., Yi T. F., Li H. Z., Zhou S. B., Chen L. E., 2008, AJ, 135, 2212
Zanotti O., Rezzolla L., Font J. A., 2003, MNRAS, 341, 832
Zhao W., Hong X. Y., An T., Jiang D. R., Zhao J. -H., Gurvits L. I., Yang J., 2011, A&A, 529, 113

This paper has been typeset from a TEX/LATEX file prepared by the author.